

See discussions, stats, and author profiles for this publication at: <https://www.researchgate.net/publication/236217674>

Concomitant Metal Organic Frameworks of Cobalt(II) and 3-(4-Pyridyl)benzoate: Optimized Synthetic Conditions of Solvatochromic and Thermochromic Systems

ARTICLE in CRYSTAL GROWTH & DESIGN · FEBRUARY 2013

Impact Factor: 4.89 · DOI: 10.1021/cg301312v

CITATIONS

16

READS

59

4 AUTHORS, INCLUDING:



Gift Mehlana

University of Cape Town

13 PUBLICATIONS 40 CITATIONS

SEE PROFILE



Gaëlle Ramon

University of Cape Town

22 PUBLICATIONS 100 CITATIONS

SEE PROFILE



Lars Öhrström

Chalmers University of Technology

131 PUBLICATIONS 1,836 CITATIONS

SEE PROFILE

Concomitant Metal Organic Frameworks of Cobalt(II) and 3-(4-Pyridyl)benzoate: Optimized Synthetic Conditions of Solvatochromic and Thermochromic Systems

Published as part of the *Crystal Growth & Design* virtual special issue In Honor of Prof. G. R. Desiraju

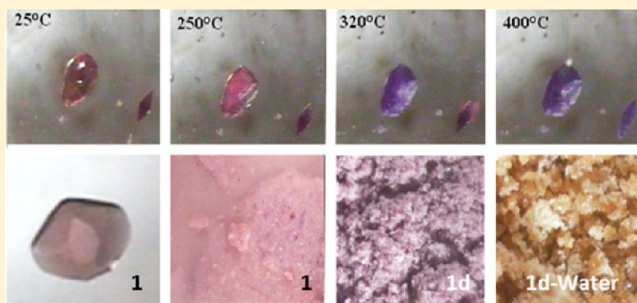
Gift Mehlana,[†] Susan A. Bourne,[†] Gaëlle Ramon,^{*,†} and Lars Öhrström[‡]

[†]Centre for Supramolecular Chemistry Research, Department of Chemistry, University of Cape Town, Rondebosch 7701, South Africa

[‡]Department of Chemical and Biological Engineering, Chalmers University of Technology, SE-412 96 Gothenburg, Sweden

S Supporting Information

ABSTRACT: Two coordination networks, $\{[\text{Co}(34\text{pba})_2]\cdot\text{DMF}\}_n$ (**1** and **2**), where 34pba is 3-(4-pyridyl)benzoate, were prepared by solvothermal methods. **1** is a three-dimensional metal organic framework formed by linking $[\text{Co}_2(34\text{pba})_8]$ clusters in a **bcu** net. **2** consists of single $[\text{Co}(34\text{pba})_4]$ units in a tetragonal plane net of **sql** topology. The thermal conditions leading to their selective synthesis were established: 120 °C for **1** and 75 °C for **2**. Their structures were solved and their thermal behavior was investigated. Further experiments established the activation energy for the desorption of the DMF molecules entrapped in their framework: 76(6)–106(16) kJ mol^{−1} for **1** and 49(3)–58(3) kJ mol^{−1} for **2**. For **1**, sorption experiments were carried out to demonstrate the ability of the coordination network to absorb different solvents, and the framework solvatochromic response was also ascertained.



INTRODUCTION

Metal organic frameworks (MOFs) present networks with varying dimensionality and porosity. Their porous architecture affords multiple applications spanning from separation to gas storage among others.^{1–3} One typical illustration is their use as sensors whereby the absorption of solvent vapors by the network results in the sensor's color change. Often, this phenomenon called solvatochromism is the result of an alteration in the metal coordination geometry or modification in the framework structure which affects the MLCT, d–d, and $\pi\cdots\pi^*$ transitions.^{4,5} Since the 1990s, the study of the design of MOFs has rapidly progressed in order to develop a rational way to grow materials with desired properties. Although the prediction of crystal structures remains difficult, their crystal engineering can be attempted through the careful choice of their building blocks and specific synthetic conditions. In the choice of the former, the metal centers (with regards to their coordination pattern and counterions), the ligand geometry and flexibility, as well as the nature of the solvent (as coordinating entity, included guest or templating agent) have to be considered since they influence the material dimensionality.^{6,7} The more flexible the ligand, the less predictable the structure; the longer the ligand, the more likely the interpenetration.^{8,9} These results indicate a constant competition between our aspiration to create materials with high porosity

and nature's abhorrence for emptiness. Among the synthetic conditions, factors such as time of reaction, pH,^{10–12} and temperature^{13–16} have been investigated.

When synthesizing coordination networks, even when starting from the same reactants, the MOFs commonly obtained are often different in their connectivity and their relative composition may also vary. Supramolecular isomerism is the term used to describe the occurrence of MOFs which possess the same chemical composition for their networks while the solvent or guest content of these networks need not be the same. Polymorph, on the other hand, is a stricter term used for any one or a combination of compounds which possesses the ability to crystallize in at least two different arrangements with identical connectivity and chemical composition of the crystals. While polymorphs in MOFs remain an uncommon phenomenon,^{17–20} the occurrence of supramolecular isomers in coordination networks has become more common as reported in recent reviews.^{21–24}

Here we report two complexes of $\{[\text{Co}(34\text{pba})_2]\cdot\text{DMF}\}_n$ (**1** and **2**), where 34pba is 3-(4-pyridyl)benzoate, which were first obtained concomitantly. These complexes although they have

Received: September 9, 2012

Revised: December 13, 2012

the same empirical formula are neither polymorphs nor supramolecular isomers as their coordination entities differ. Thus, the molecular building blocks (MBB) in **1** and **2** are different, and the compounds obtained may be described as MBB structural isomers.

By varying the synthetic conditions, selective production of one form (or the other) is achieved. Both crystal structures were solved and their topology was investigated so as to understand the difference in their thermal behavior. Pyridine carboxylate MOFs inherit aspects of both early coordination polymers, such as those based on 4,4'-bipyridine, and the carboxylates MOFs, such as Yaghi's MOF-5, and is one reason that terminology in this area needs to be inclusive rather than restrictive.²⁵ The kinetics of DMF desorption were studied for **1** and **2**. The thermochromism of both compounds is also described and the reason behind the color change occurring at high temperatures is elucidated. Using **1** as a sensing material, its solvatochromic properties were established and absorption of various solvents was carried out successfully.

■ EXPERIMENTAL SECTION

All materials were purchased from commercial sources and used without further purification; all solvents were dried over molecular sieves.

Crystal Growth. Synthesis of $\{[\text{Co}(\text{34pba})_2] \cdot \text{DMF}\}_n$: 29 mg (0.1 mmol) of cobalt nitrate, $\text{Co}(\text{NO}_3)_2 \cdot 6\text{H}_2\text{O}$, was dissolved in 2 mL of methanol. 80 mg (0.4 mmol) of 3-(4-pyridyl)benzoic acid was dissolved separately in 5 mL of dimethylformamide (DMF) under stirring and heating. The two solutions were mixed and the resulting solution was placed in an autoclave, tightly sealed, and heated in an oven for 24 h at 105 °C. Crystals were obtained upon slow cooling of the reaction mixture to room temperature. Two crystal forms were identified based on their shape and color: the major product (1) consisted of large light-purple crystals, while the minor product (2) consisted of a few smaller dark-purple diamond-shaped crystals.

The use of high temperatures in the synthetic process normally favors thermodynamic products while low temperatures favor kinetic products. The synthetic conditions leading to each product were refined in order to obtain the desired compound selectively. Using the same concentrations as before, but in the presence of molecular sieves to capture the water liberated by the cobalt salt, the synthesis was carried out at 75 °C for 24 h. A mixture of **2** and another crystalline compound (**3**) was obtained but due to the poor crystallinity of compound **3**, it was not possible to fully characterize it. The synthesis of **2** could not be optimized further, and to carry out any additional experiments, **2** had to be separated manually from **3** under a microscope. On the other hand, higher temperatures (120 °C) and the same concentration led to the formation of **1** exclusively.

Crystal Structure Determination. Crystal structure determinations were performed by single crystal X-ray diffraction using a Bruker KAPPA APEX II DUO diffractometer with graphite monochromated Mo- $K\alpha$ radiation ($\lambda = 0.71073$ Å). The data collections were carried out at low temperature (173 K) using a Cryostream cooler (Oxford Cryosystems UK). Unit cell refinement and data reduction were performed using the program SAINT.²⁶ Data were corrected for Lorentz-polarization effects and for absorption (program SADABS²⁷). Structure solutions were achieved by direct methods (program SHELXS²⁸) and refined by full-matrix least-squares on F^2 with anisotropic thermal parameters for all non-hydrogen atoms using SHELXL²⁹ within the X-SEED³⁰ interface. The non-hydrogen atoms were located in the difference electron density maps and were refined anisotropically, while all the hydrogen atoms were placed with geometric constraints and refined with isotropic temperature factors. The crystal data and refinement parameters are detailed in Table 1. The material concerning the structures (CIF files) is available free of charge via the Internet at <http://pubs.acs.org>. The structures were

Table 1. Crystal Data and Refinement Parameters

	1: [[Co(34pba) ₂].DMF] _n	2: [[Co(34pba) ₂].DMF] _n
molecular formula	C ₂₇ H ₂₃ CoN ₃ O ₅	C ₂₇ H ₂₃ CoN ₃ O ₅
molecular mass/g mol ⁻¹	528.41	528.41
crystal size (mm)	0.16 × 0.18 × 0.33	0.17 × 0.17 × 0.39
temp of collection/K	173	173
crystal symmetry	orthorhombic	tetragonal
space group	<i>Pbca</i>	<i>P</i> ₄ ₃ ₂ ₁ ²
<i>a</i> /Å	18.0941(7)	11.4957(8)
<i>b</i> /Å	14.3903(6)	11.4957(8)
<i>c</i> /Å	19.1497(8)	37.257(4)
<i>V</i> /Å ³	4986.2(4)	4923.6(3)
<i>Z</i>	8	8
<i>D_c</i> /g cm ⁻³	1.408	1.423
<i>μ</i> (Mo–Kα)/mm ⁻¹	0.731	0.740
<i>F</i> (000)	2184	2176
range scanned, <i>θ</i> /°	2.1–28.3	1.9–28.3
index ranges (<i>h</i> , <i>k</i> , <i>l</i>)	–13: 24; –16: 19; –18: 25	–14: 15; –15: 15; –29: 49
no. reflections collected	20171	42251
no. unique reflections	6183	6166
no. reflections with <i>I</i> > 2σ(<i>I</i>)	4642	5272
data/parameters refined	6183/327	6166/374
goodness of fit, <i>S</i>	1.00	1.19
final <i>R</i> indices (<i>I</i> > 2σ(<i>I</i>))	0.0364	0.0658
final <i>wR</i> ₂ (all data)	0.0949	0.1432
min, max <i>e</i> density/ <i>e</i> Å ⁻³	–0.34, 0.43	–0.61, 0.35
Flack parameter	N/A	0.12 (3)

deposited at the Cambridge Crystallographic Data Centre and allocated the numbers: CCDC 894482 and 894483.

The geometry and volume of the network cavities were modeled using MERCURY.³¹

Topology Studies. The networks in 1 and 2 were analyzed using SYSTRE³² and TOPOS³³ and checked against the Reticular Chemistry Structural Resource (RSCR).³⁴ The relevant output files are available in Supporting Information.

For **1**, the calculated point symbol and vertex symbol were found to be $4^{24}.6^4$ and $[4.4.4.4.4.4.4.4.4.4.4.4.4.4_3.4_3.4_3.4_3.4_3.4_3.4_3.4_3.4_3.4_3.4_3.*.*.*]$ respectively. The calculated topological density value (TD10) was found to be 2331.

For 2, the point symbol was established as $4^4.6^2$ and extended point symbol as 4.4.4.4.6₂.6₂ while the vertex symbol was determined as [4.4.4.4*.]. The calculated topological density value (TD10) was found to be 221.

Hot Stage Microscopy. The thermal behaviors of compounds **1** and **2** were monitored using a Nikon SMZ-10 stereoscopic microscope fitted with a Linkam THMS600 hot stage and a Linkam TP92 temperature control unit. The samples were placed on a glass slide, covered in silicon oil and heated at a rate of $10\text{ }^{\circ}\text{C min}^{-1}$. The process was followed using a Sony Digital HAD color video camera and recorded using the Soft Imaging System program.³⁵

Differential Scanning Calorimetry (DSC). Differential scanning calorimetry (DSC) was performed using a TA Instrument DSC-Q200 on 1–2 mg samples placed in aluminum cells with vented lids and heated at 10 °C min⁻¹ under nitrogen gas flow (50 mL min⁻¹).

Thermogravimetric Analysis (TGA). Thermogravimetric analyses (TGA) were recorded using a TA Instrument TA-Q500 on 1–2 mg samples under nitrogen gas flow (50 mL min^{-1}) at a heating rate of $10 \text{ }^{\circ}\text{C min}^{-1}$.

Kinetics. Nonisothermal desorption kinetic studies were performed on the TA Instrument TA-Q500. For both compounds **1** and **2**, TG traces of the DMF desorption were recorded at different heating rates (4.0, 8.0, 16.0, and 32.0 °C min⁻¹). The data were analyzed using the

Universal analysis specialty program³⁶ to obtain the percentage conversion level at a given temperature. From these, the activation energy (E_a) for the desorption of the DMF molecules in **1** and **2** was derived, as described in the Results.

Powder X-ray Diffraction (PXRD). Powder X-ray diffraction (PXRD) patterns were recorded using a HUBER Imaging Plate Guinier Camera 670 using Ni-filtered Cu-K α radiation ($\lambda = 1.5406$ Å) generated by a Philips X-ray generator at 20 mA and 40 kV. The sample crystals were applied directly onto Mylar film or placed in a capillary tube and exposed to the radiation for 60 min with 10 multiscans to collect the data. A HUBER High-Temperature Controller HTC 9634 unit was used with a capillary rotation device when generating PXRD patterns at elevated temperatures.

Infrared. IR studies were performed on a Perkin-Elmer Spectrum 100FT-IR using KBr pellets over a range of 4000 cm⁻¹ to 450 cm⁻¹.

RESULTS AND DISCUSSION

Synthesis. At first, the crystals of the two compounds occurred in the same vial and were identified due to their different shapes and colors. The major product, **1**, consisted of large light-purple truncated prisms, while **2**, the minor product, consisted of small dark-purple diamond-shaped crystals (Figure 1).

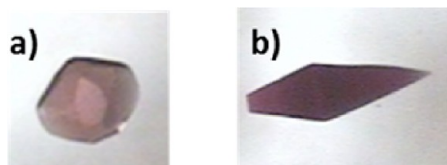


Figure 1. Crystals of the two isomers of $\{[\text{Co}(\text{34pba})_2]\cdot\text{DMF}\}_n$: (a) **1**; (b) **2**.

In an attempt to determine the optimal conditions to yield selectively one compound over the other, we carried out synthetic experiments at various temperatures ranging from 75 to 120 °C. For each set of experiments we identified the

composition of the material obtained by visual inspection and by measuring the PXRD trace of the products (Figure 2).

At 120 °C, **1** is obtained selectively. At 105 °C, the synthesis results in a mixture of **1** and **2** with only a few crystals of **2** present, thus the similar PXRD to that at 120 °C. At 75 °C, the raw material comprises both compounds **2** and **3**, although **2** remains a minor compound. Since, in general, high temperature favors thermodynamic products,^{14,37} we hypothesize that **1** is the thermodynamically stable compound (synthetic conditions: 120 °C) while **2** is a kinetic product (synthetic conditions: 75 °C).

However, in the particular case of concomitant crystallization,³⁸ it is difficult to confirm, using the usual analytical techniques, which of the products is the thermodynamic or the kinetic material since they are (almost) energetically equivalent. This arises from the fact that concomitant crystals form in a domain where their crystallization areas overlap. This results in a subtle balance between the factors governing the formations of the two crystalline forms. Finally, seeing that the isomers were obtained using solvothermal techniques, not only should the influence of temperature be considered but also that of the pressure.

Crystal Structure of $\{[\text{Co}(\text{34pba})_2]\cdot\text{DMF}\}_n$. **1** crystallizes in the orthorhombic crystal system and space group *Pbca*. The asymmetric unit consists of one metal center Co(II) coordinated to two deprotonated 34pba ligands, A and B belonging to the network, and one uncoordinated DMF solvent molecule as guest. Ligand B bridges two Co(II) ions to form a $\text{Co}_2(\text{34pba})_8$ cluster. The geometry of the metal centers in the network is distorted octahedral with each Co(II) coordinating to five ligands. Two Co(II)-N(pyridyl) bonds are in axial positions, while the equatorial positions have Co(II)-O-(carboxylate) bonds: two single Co(II)-O and one bidentate Co(II)-O bond. The two ligands singly bonded via Co(II)-O to the first metal center are also involved in coordinating the adjacent metal center through single Co(II)-O with the

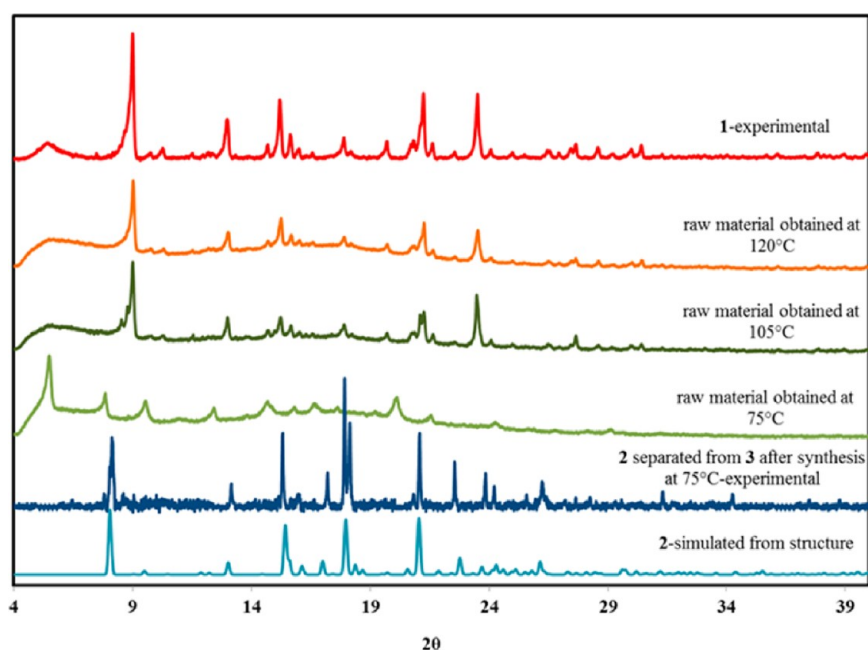


Figure 2. PXRD analysis of the raw materials obtained at different temperatures.

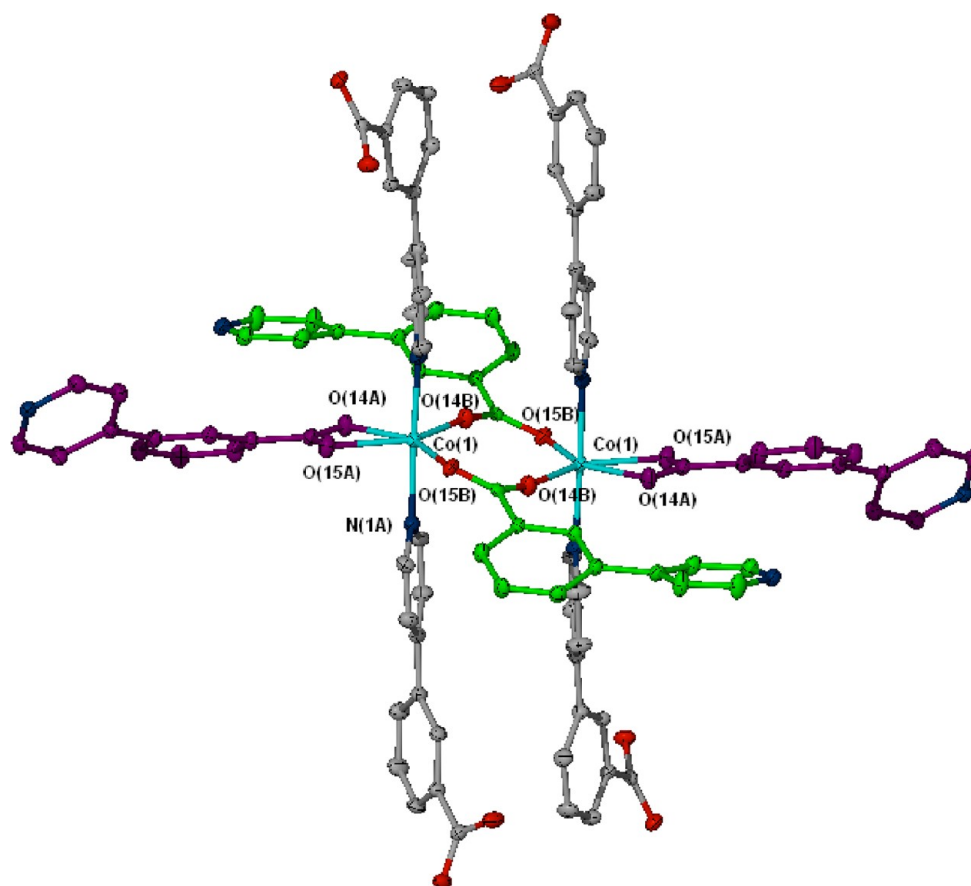


Figure 3. 1: Coordination geometry of the Co(II) centers displaying Co(II)–N bonds in axial position (ligands in gray) and Co(II)–O in equatorial positions (ligands in purple and green). Each metal center bonds to three ligands via one bidentate Co(II)–O bond (in purple) and via two single Co(II)–O bond (in green). The two Co(II) centers are bridged via O(15B)–C(13B)–O(14B).

second oxygen atom of their carboxylate moiety (Figure 3, Tables S1 and S2).

This gives rise to a neutral 3D-network with interstitial cavities where DMF molecules reside (Figures 4 and 5c). The

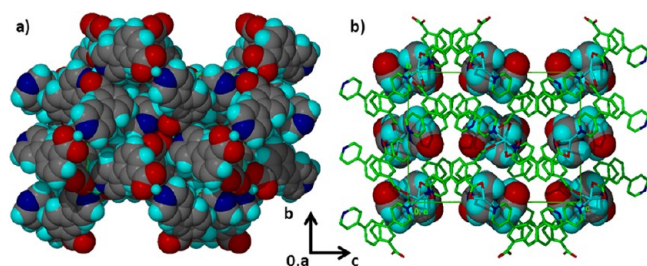


Figure 4. Packing of **1** view along [100] displaying: (a) the 3D-network in van der Waals radii and the DMF molecules omitted for clarity, (b) the coordination network in green and the DMF molecules (in van der Waals radii) residing in cavities (the network hydrogen atoms were omitted for clarity).

DMF molecules in the cavities are pairwise stacked and the interplanar distance between the DMF measured as 3.62 Å. As long as the solvent molecules are in place, the material **1** is nonporous.

Each node, placed at the center of the $[\text{Co}_2(34\text{pba})_8]$ cluster, is 8-connected. Topological analysis of this network by TOPOS revealed a near-ideal **bcu** net (Figure 5).

There are no notable intermolecular interactions stabilizing the guest molecules inside the cavities. However, weak intramolecular C–H...O hydrogen bonding interactions exist in the framework (Table S3).

Crystal Structure of $\{[\text{Co}(34\text{pba})_2]\cdot\text{DMF}\}_n$, **2.** **2** crystallizes in the tetragonal crystal system and space group $P4_32_12$. The asymmetric unit consists of one Co(II) center and two deprotonated ligands (A and B) constituting the MOF, while one uncoordinated DMF molecule occupies its voids. The pyridyl moiety of one ligand (A) is disordered over two positions with site occupancies of 0.55 for the A2 fragment and 0.45 for the A1 fragment. The DMF molecule is disordered over two positions with site occupancies of 0.6 for O(1C1) and 0.4 for O(1C2). The disorder, which was satisfactorily modeled, is displayed in Figure 6.

The Co(II) center has a distorted octahedral geometry, bonding to four ligands through two bidentate Co(II)–O(carboxylate) bonds and two single Co(II)–N(pyridyl) bonds (Figure 6, Tables S4 and S5).

The network is a simple square grid with topology symbol **sql** (Figure 7).

The packing of **2** displays interdigitated layers resulting in a 2D-network in the cavities of which DMF molecules reside (Figure 8). As long as the solvent molecules are in place, the material **2** is nonporous. As in **1**, there are no intermolecular interactions stabilizing the guest molecules within the network although adjacent 2D-layers are connected via weak intermolecular C–H...O hydrogen bonds (Table S6).

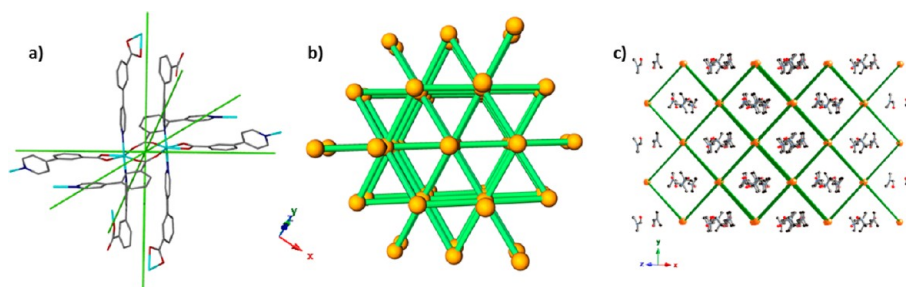


Figure 5. (a) Network connectivity of **1**. (b) Network analysis of compound **1**. Orange spheres represent the 8-connected uninodal node at the $\text{Co}_2\text{C}_2\text{O}_4$ cluster, (c) the **bcu** net in **1** drawn with the guest molecules in the cavities.

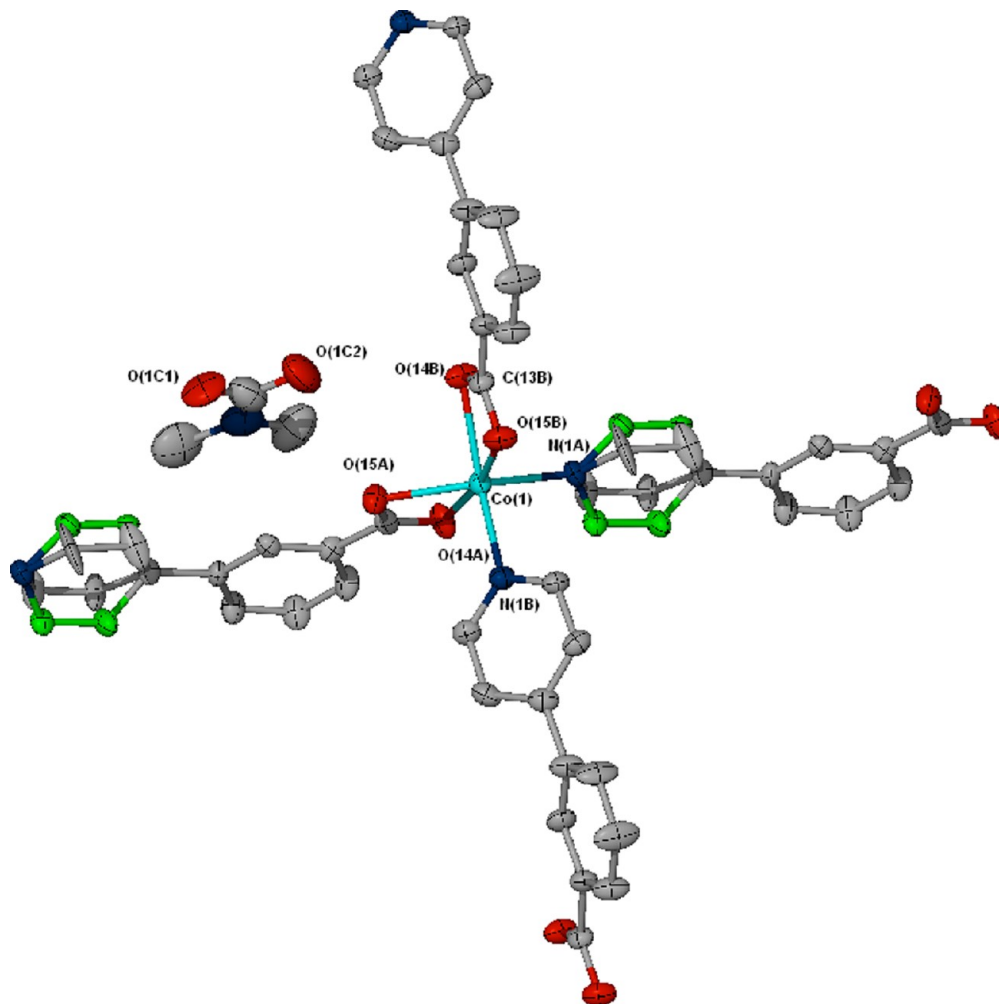


Figure 6. 2: Geometry around the Co(II) center displaying the disorder in ligand A (in green) and DMF molecule. Hydrogen atoms are omitted for clarity.

Thermal Analysis and Thermochromism. The thermal behavior of each compound was investigated and they were compared using TGA and DSC (Table 2, Figures S1 and S2).

On the TGA, the desorption of the DMF molecules occurs over different temperature ranges: 100–280 °C for **1** (associated with a broad endothermic peak at 191 °C on the DSC), while the same phenomenon takes place from 50 to 175 °C for **2** with an endothermic peak at 134 °C in the DSC. This can be explained by the structural features of the compounds. In neither of the two compounds are the DMF molecules held in the structures via stabilizing bonds but are rather confined in pockets. In **1**, the DMF molecules are contained in cavities of

the 3D-network which is rigid and tightly encloses them. In **2**, the network consists of interdigitated layers which may glide to release the solvent molecules, resulting in the lower temperature of desorption. Alongside the endothermic peaks associated with the desorption of the solvent and that of melting (at 408 °C for **1** and 405 °C for **2**), the DSC traces of **1** and **2** each display an exotherm, at 281 and 347 °C respectively. The events were investigated with hot stage microscopy (HSM) (Figure 9) and PXRD (Figure 10).

The PXRD traces of **1** at various temperatures show that **1** maintains its structure (even after DMF is desorbed) until 240 °C. After 240 °C, **1** undergoes an irreversible phase transition,

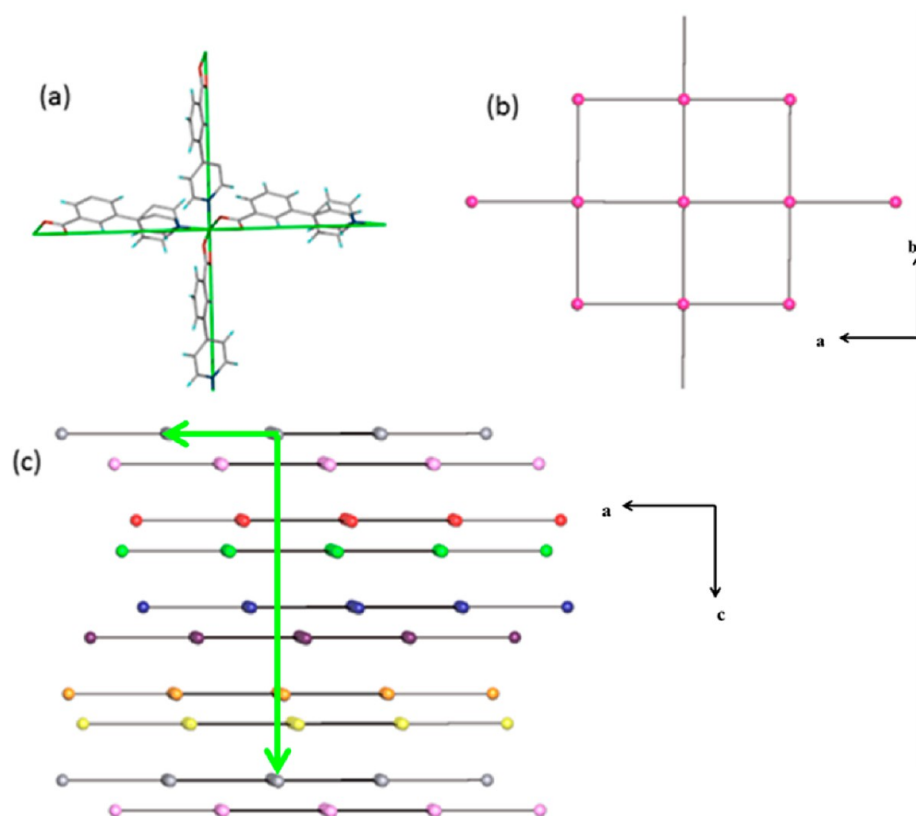


Figure 7. (a) Network connectivity of **2**. (b) Network analysis of compound **2**. Each pink sphere represents the 4-connected node at the Co(II) ion. (c) Parallel tetragonal plane nets found in **2** (long c axis of 37.257(4) Å).

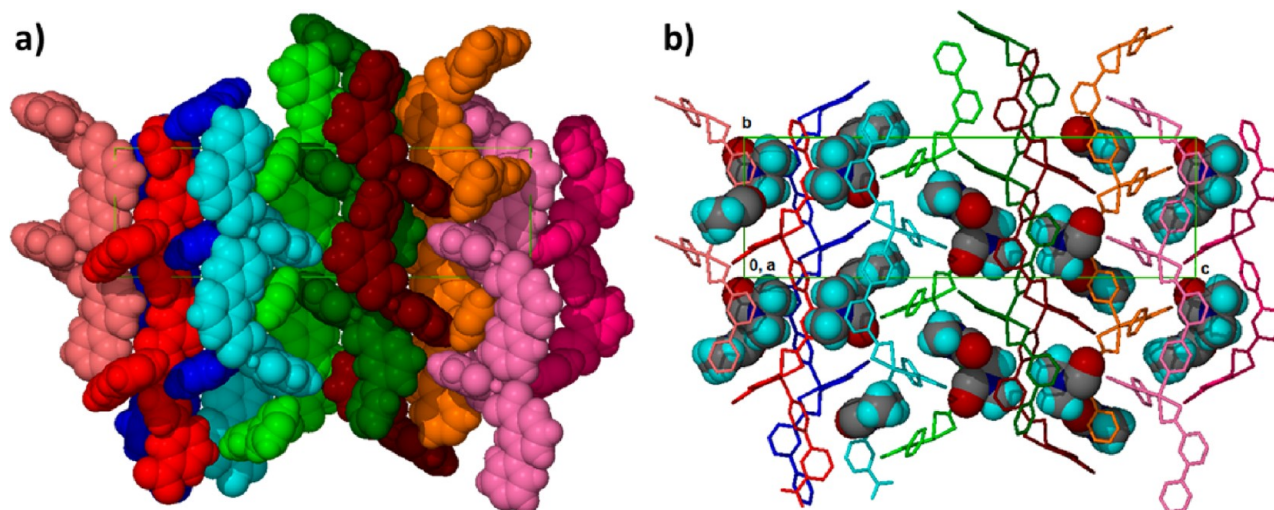


Figure 8. Packing of **2** viewed down $[100]$: (a) 2D-network from interdigitated layers represented in van der Waals radii with the disorders and the DMF molecules omitted for clarity, (b) coordination network in sticks displaying the pockets containing the DMF molecules (van der Waals radii).

the structure of which is retained after the compound is cooled to room temperature. The pattern calculated from the crystal structure of **1** was compared to its experimental trace. The two patterns match proving that the bulk material consists only of **1**. The slight shift between the peaks of the calculated and experimental patterns is due to the difference in temperature between the single crystal structure determination and the experimental PXRD.

Although the two compounds possess different structural features and display different thermal behavior toward their

guest, they both present a phase transition at high temperature (281 °C for **1** and 347 °C for **2**) associated with a color change to blue. Insufficient material precluded PXRD studies on **2**; however for **1** this transition is irreversible and the new phase remains upon cooling to room temperature. Regrettably, the compound did not stay crystalline enough to allow for single crystal data collection. The melting points of **1** and **2** after the exothermic phase transition differ by ca. 3 °C. We repeated the DSC at a heating rate of 2 °C min⁻¹ but the difference in melting point remained constant. For cobalt compounds, the

Table 2. Thermal Analysis (TGA and DSC) for 1 and 2 as well as the Compounds Resulting from Sorption Studies: 1d, 1d-Water, 1d-MeOH, 1d-EtOH, 1d-Acetone and 1d-DMF

	TG analysis			DSC analysis			
	experimental mass loss (%) with corresponding calculated network: solvent ratio based on Co(34pba) ₂ :x ^a			T _S (°C): solvent desorption	T _T (°C): transition phase	T _M (°C): melting	T _b (solvent) (°C)
			temperature range of mass loss				
1	14.3	1:1.0	100–280	191	281	408	DMF: 152–154
2	14.2	1:1.0	50–175	134	347	405	DMF: 152–154
1d					284	407	
1d-Water	15.4	1:4.6	RT ^b –175	120	263	not recorded	H ₂ O: 100.0
1d-MeOH	10.3	1:1.6	RT ^b –90	61	283	406	MeOH: 65.0
1d-EtOH	9.9	1:1.1	RT ^b –175	144	271	not recorded	EtOH: 78.4
1d-Acetone	8.5	1:0.7	RT ^b –235	184 (broad)	283	406	acetone: 56–57
1d-DMF	14.8	1:1.1	100–270	188	287	not recorded	DMF: 152–154

^aThe network:solvent ratios were calculated using the experimental results of the TGA for all compounds. The results were modeled on $[\text{Co}(\text{34pba})_2] \cdot \text{solvent}_x$ and expressed as 1:x. ^bRT: room temperature.

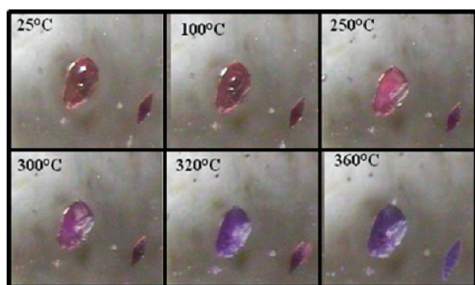


Figure 9. Hot stage microscopy of 1 (large crystal) and 2 (small crystal). There is a slight color change in 1 after solvent desorption (250 °C). The phase transition which was observed by DSC is accompanied by a more noticeable color change of each of the crystals after the event: at 300–320 °C for 1 and at ca. 350–360 °C for 2.

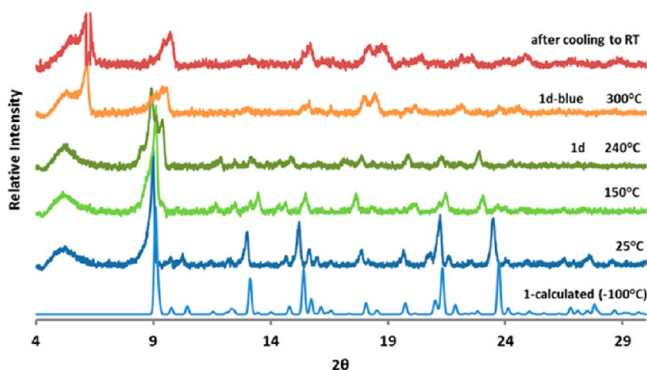


Figure 10. PXRD of 1 at various temperatures showing the phase transition upon heating.

colors, blue and purple, have been documented as corresponding to different coordination geometries³⁹ with blue being associated with the tetrahedral geometry. For this reason, we surmise that the color change we observe for our compounds is the result of a change in coordination geometry from octahedral (observed in the crystal structures) to tetrahedral. This was further confirmed by comparing the infrared spectra of the ligand 34pba, compounds 1, 1d (purple in color, obtained from 1 after desorption of the solvent at 150 °C) and

1d-blue (blue in color, after 1 is heated above 290 °C) as well as comparing compound 2 (purple in color, as made) with 2d-blue (blue in color, after 2 has undergone phase transition) (Figure 11).

The band at 1675 cm⁻¹ in 34pba was assigned to the carbonyl stretch of the ligand while that in 1 was assigned to the carbonyl stretch of the DMF molecule (no ligand carbonyl group remained due to the coordination in the framework). This band is absent in 1d and 1d-blue, as the DMF has been desorbed. The stretches at 1613 cm⁻¹ in all the compounds were assigned to the conjugated C–C of the benzene rings. The asymmetric and symmetric stretches of the carboxylate were observed at 1550 and 1391 cm⁻¹ respectively in 34pba, compounds 1 and 1d with a magnitude of separation between the carboxylate stretches of 159 cm⁻¹. In 1d-blue, the asymmetric and symmetric carboxylate stretches were located at 1570 and 1394 cm⁻¹ respectively, and the magnitude of separation was found to be 176 cm⁻¹. In compound 2, the asymmetric and symmetric stretches of the carboxylate were observed at 1546 and 1395 cm⁻¹ respectively with a magnitude of separation between the carboxylate stretches of 151 cm⁻¹. In 2d-blue, the asymmetric and symmetric carboxylate stretches were located at 1570 and 1384 cm⁻¹ respectively, and the magnitude of separation was found to be 186 cm⁻¹.

There is precedence in the literature that the magnitude of separation (Δ) between the asymmetric and symmetric carboxylate stretches be used as spectroscopic criteria to determine the mode of the carboxylate binding.^{40,41} Generally, the following order is proposed for divalent metal carboxylates: $\Delta(\text{chelating}) < \Delta(\text{bridging}) < \Delta(\text{ionic}) < \Delta(\text{monodentate})$. From the IR results, it can be argued that the thermochromic effect exhibited by both 1 and 2 is due to change in the binding mode of the carboxylate group from bidentate to monodentate (and from octahedral to tetrahedral coordination) confirming our hypothesis that the change in color is directly related to a change in geometry.

Desorption Kinetics. The kinetics of DMF desorption were studied for 1 and 2. A model-free isoconversional method based on the Ozawa, Flynn and Wall^{42,43} method was used to determine the activation energy related to the results obtained from the nonisothermal TGA. This method relies on the use of

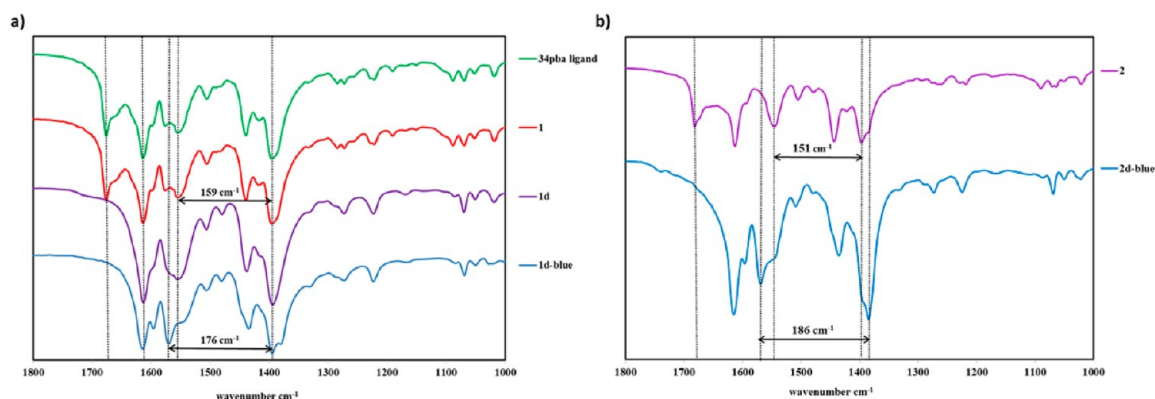


Figure 11. Infrared spectra: (a) 34pba ligand, **1**, **1d**, and **1d-blue** and (b) **2** and **2d-blue** displaying the positions of the peaks which allow one to characterize the coordination modes in the frameworks.

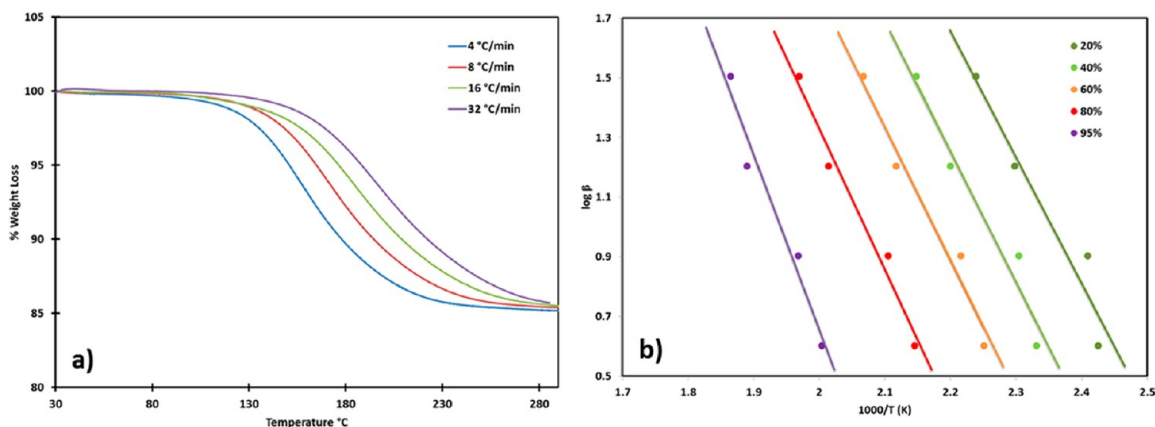


Figure 12. Desorption kinetics for **1**: (a) Desorption traces obtained from the non-isothermal runs, (b) $\log \beta$ versus $1/T$, the slope of which ensued the activation energies at the different conversion levels.

several heating rates and the temperatures being recorded at specific conversion rates for each heating rate. The conversion levels are defined in terms of percentages based on the extent-of-reaction (α). Equation 1 allows the determination of the activation energies at each conversion level, where β_α is the heating rate, A_α is the frequency factor, $E_{a\alpha}$ is the activation energy, T_α is the temperature at each conversion level, and $g(\alpha)$ refers to the kinetic model. The TGA traces were converted to extent-of-reaction (α) versus temperature curves. From these curves, $\log \beta_\alpha$ versus $1/T_\alpha$ were established (Figures 12 and S3).

$$\log \beta_\alpha = \log \left(\frac{A_\alpha E_{a\alpha}}{g(\alpha)R} \right) - 2.315 - 0.457 \left(\frac{E_{a\alpha}}{RT_\alpha} \right) \quad (1)$$

The use of non-isothermal methods allows for the determination of the activation energy only, while the mechanism of desorption cannot be identified. The activation energy (E_a) obtained for **1** ranges from 76(6) to 106(16) kJ mol^{-1} for 20 to 95% conversion levels (average 86(9) kJ mol^{-1}), while for **2**, $E_a = 49(3)$ to 58(3) kJ mol^{-1} (average 53(4) kJ mol^{-1}) for the same conversion level range (Table S7). Although we note that the activation energy increases concurrently with the conversion levels, it should be borne in mind that the activation energies calculated from these experiments correspond to the full desorption process. That the values have relatively low percentage errors suggests that the mechanism of desolvation is a fairly constant process.

The activation energies for the kinetics of solvent desorption may be considered with respect to the crystal packing of the compounds (cages, open or constricted channels or layers), the interactions between the solvent and the framework in which it is entrapped (hydrogen bonding or other weak interactions), the amount (framework:solvent) and nature (boiling point) of the solvent included. Although this is a complex process, our results for **1** compare well with those previously reported in the literature, where activation energies are reported over the range 75–160 kJ mol^{-1} .^{44–46} Furthermore, the values of the activation energy obtained for the desorption of DMF for **1** and **2** concur with the conclusions drawn from the thermal analyses and the features of the crystal networks whereby the DMF molecules were described as tightly held inside the framework of **1** while those entrapped in the framework of **2** were held more loosely as a result of the 2D-layers which may glide past one another.

Solvatochromism. Earlier we reported the formation of coordination networks such as $\{[M_4(44pba)_8] \cdot \text{solvent}\}_n$ 3D-frameworks of 4-(4-pyridyl) benzoate (44pba) with Co(II) and Ni(II) metal centers.⁴⁷ These frameworks were porous upon desorption of the solvent with wide channels capable of accommodating different solvent molecules. The cobalt compound demonstrated solvatochromic properties upon absorption of various solvents. Originally purple in color, the material displayed color change ranging from yellow to pink depending on the polarity and protic nature of the solvent absorbed. Since 34pba is an isomer of 44pba, similar sorption

studies were carried out on **1**. The sorption experiments could not be carried out on **2** as it was not possible to synthesize the material in sufficient quantity.

The compound **1d** was obtained after heating **1** at 150 °C for 10 h under vacuum. The compound turned from light to dark purple in the process and consisted of the desolvated coordination network of **1** (Table 2, Figure S4). The space originally occupied in **1** by the guest molecules was left vacant and the resulting material, **1d**, is porous. **1d** was soaked for 24 h in water, methanol, ethanol, acetone, and DMF to generate **1d-Water**, **1d-MeOH**, **1d-EtOH**, **1d-Acetone**, and **1d-DMF** respectively. All retained the original purple color of **1d** except **1d-DMF** which appears the same light purple as **1** and **1d-Water** which turned bright yellow (Figure 13).

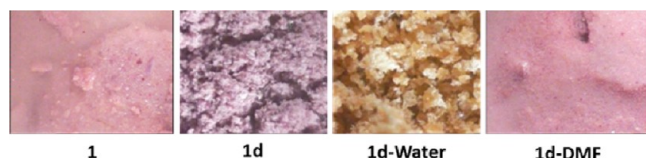


Figure 13. Solvatochromic properties of **1**: the 3D-coordination network displays different colors according to the solvent it entraps.

Powdered samples of **1d** were exposed to solvent vapors at room temperature for a period of 24 h in a controlled environment. The resulting compounds **1d-solvent** were characterized using thermal analyses to establish the amount of solvent enclathrated in the framework (Table 2 and Figures S5–S9) and their PXRD recorded (Figure 14).

The PXRD traces exhibit the structural changes which the network undergoes in the process of desorption (**1d**) and solvent absorption, demonstrating that the 3D-network possesses a degree of flexibility. The network adapts to its environment and none of the PXRD patterns are the same, starting with **1d** which not only displays a different PXRD trace but also a different color to **1**. The resilience of the network was confirmed after **1d** was exposed to DMF vapors and the

resulting product: **1d-DMF** exhibited the same PXRD pattern and color as those originally obtained for **1**. In the case of **1d-Water**, the changes resulting from the absorption of water by the network are drastic in that the material not only turns bright yellow but also loses part of its crystallinity. This phenomenon has been previously observed and can be explained by the ability of the solvent to form hydrogen bonds which cause molecular distortion of the network and affect the energy of MLCT, $\pi\cdots\pi^*$, and d-d transitions.^{4,5,47}

To investigate the absorption of solvents by our frameworks, the geometry and volume of the cavities were modeled. Although the absorption experiments were not carried out with compound **2**, study of its solvent available voids are also reported.

In both compound **1** and **2**, the coordination frameworks contain voids in which solvent molecules reside. We demonstrated that for **1** these solvent molecules can be desorbed and the framework can then be subsequently loaded upon exposure to various solvent vapors. The loading capacity was estimated using the formula:

$$\text{loading capacity} = \frac{\text{solvent accessible volume}}{Z \times \text{molecular volume}} \quad (2)$$

where solvent accessible volumes were estimated using Mercury with a probe radius of 1.2 Å and a grid step of 0.2 Å. For **1**, the solvent accessible volume was found to be 1387 Å³ and for **2**, it is 1090 Å³ (Figure 15).

The molecular volume for each solvent was calculated from their liquid density:

$$\text{molecular volume} = \frac{\text{molecular weight}}{N_A \times \text{density}} \quad (3)$$

(Detailed calculations are provided in the Supporting Information.)

Comparing the available space in the framework of **1** with the solvent molecular volumes, we observed that the amount of solvent captured in the framework seemed to be directly proportional to the solvent steric hindrance (Table 3).

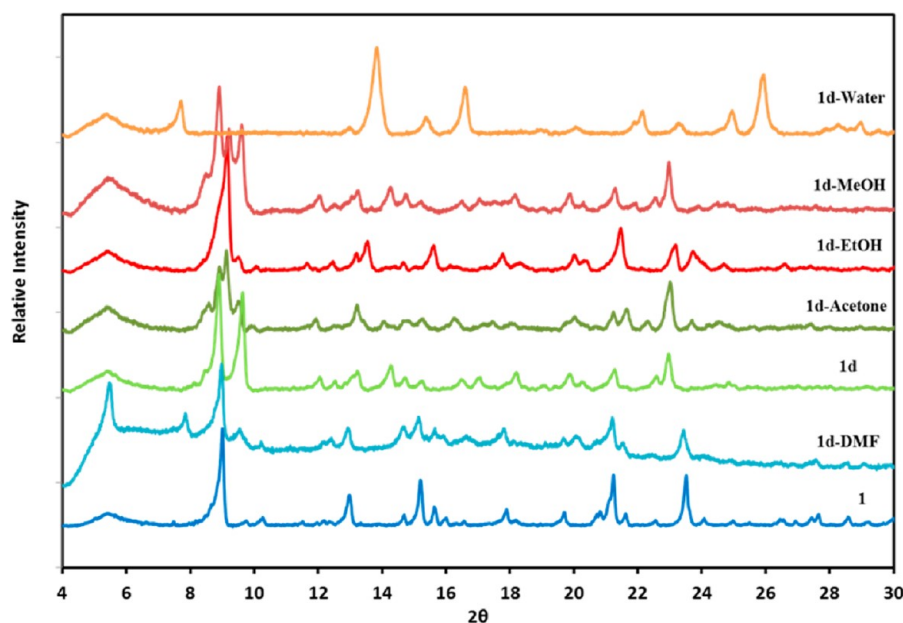


Figure 14. PXRD traces of **1**, **1d** and solvated forms of **1**.

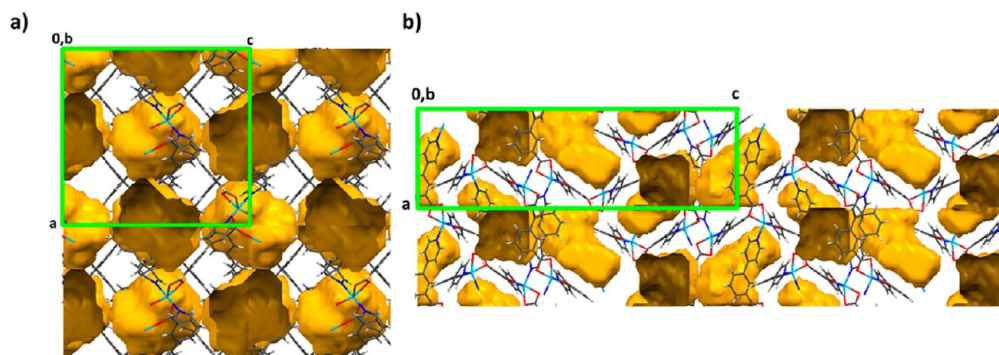


Figure 15. The networks cavities were modeled using the program Mercury and the cavities in each network displayed for (a) **1** and (b) **2**. The cavities in both networks are not interconnected but they are nevertheless in close contact. This allows for the movement of guest molecules through small modifications of the network, whose resilience we demonstrated using vapor sorption experiments.

Table 3. Experimental and Theoretical Solvent Loading of **1** Network

	TGA		solvent			
	experimental mass loss (%) with network/solvent ratio based on $\text{Co(34pba)}_2 \cdot x^a$		T_b (solvent) ($^{\circ}\text{C}$)	solvent molecular volume (\AA^3) ^b	calculated maximum load $\text{Co(34pba)}_2 \cdot x$ (% loading) ^c	
1	14.3	1:1.0	DMF	152–154		
1d						
1d-Water	15.4	1:4.6	H₂O	100.0	30	1:5.8 (79%)
1d-MeOH	10.3	1:1.6	MeOH	65.0	67	1:2.6 (62%)
1d-EtOH	9.9	1:1.1	EtOH	78.4	97	1:1.8 (61%)
1d-Acetone	8.5	1:0.7	Acetone	56–57	122	1:1.4 (50%)
1d-DMF	14.8	1:1.1	DMF	152–154	128	1:1.4 (79%)

^aThe network:solvent ratios were calculated using the experimental results of the TGA for all compounds. The results were modeled on $\{[\text{Co(34pba)}_2] \cdot \text{solvent}_x\}_n$ and expressed as 1: x . ^bSolvent molecular volumes were estimated from their liquid density. ^cChannel volume calculated using Mercury: 1387 \AA^3 .

With compound **1**, when comparing the results obtained from the vapor sorption experiments to the theoretical ‘maximum loading’ calculations (Table 3), the experimental loading appears to be consistent with the molecular volume and the boiling point of the respective solvents. For solvents with a high boiling point such as water and DMF, the loading of the network reaches results of approximately 80% loading, while for those with lower boiling points such as acetone, methanol and ethanol, the loading of the cavities varies from around 50–60%. For solvents with a low boiling point, the results are the furthest from the maximum loading capacity because at room temperature, the equilibrium between the solvent in its gaseous phase and in its enclathrated phase is in favor of the gaseous phase. This explains a poor retention in the cavities of the network. Since the sorption experiments were carried out at ambient temperature and at atmospheric pressure, such results can be expected. To obtain higher loadings, one could consider loading the network under higher pressure and/or at low temperature.

CONCLUSION

The structures of two metal organic frameworks, **1** and **2**, are reported whereby not only the composition of the frameworks, $[\text{Co(34pba)}_2]_n$ but also the content of these frameworks, $[\text{DMF}]_n$, are identical. **1**, $\{[\text{Co(34pba)}_2] \cdot \text{DMF}\}_n$, consists of a **bcu** 3D-framework encapsulating DMF molecules in pockets while **2** is a **sql** 2D-network of mobile interdigitated layers also entrapping DMF molecules. Because of their different

molecular building blocks, these compounds can be described as structural isomers.

The synthesis of both compounds was refined and it was hypothesized that **1**, produced at high temperature (120°C), is the thermodynamic product, while **2**, produced at lower temperature (75°C), is the kinetic one.

In both compounds **1** and **2**, the change of color from purple to blue, occurring at high temperature (above 290°C), was investigated using PXRD and IR. We conclude that this thermochromism is associated with a change in coordination geometry of the metal centers.

The activation energies of DMF desorption was established as from $76(6)$ to $106(16) \text{ kJ mol}^{-1}$ and from $49(3)$ to $58(3) \text{ kJ mol}^{-1}$ for **1** and **2** respectively. These values corresponded well with the structural characteristics and the thermal behaviors of the compounds.

It was furthermore observed that upon desorption of the DMF molecules, the empty framework **1d**, $[\text{Co(34pba)}_2]_n$, retained its original structure and readily absorbed methanol, ethanol, acetone and DMF while retaining its pink-purple color. However, upon absorption of water, the material displayed a dramatic color change, known as solvatochromism, from purple to bright yellow.

Because of its resilience, its ability to absorb solvent and change color, **1** demonstrates characteristics that could be exploited in the production of sensors (detection of high temperature or moisture). Sorption properties (absorption and desorption), thermochromism and solvatochromism were all

related to the crystal structures of the material and the changes it goes through during these processes. Additionally, through the identification of **2** which was fortuitous since **1** and **2** crystallized concomitantly, we were able to rationalize the conditions yielding the selective synthesis of each form.

■ ASSOCIATED CONTENT

■ Supporting Information

Tables S1–S6: bond length and angles defining the geometry of the Co(II) metal center and parameters of the weak hydrogen bonds in the coordination networks of isomers **1** and **2**, Figures S1–S2, S4–S9: thermal analyses of **1**, **2**, **1d** and solvated forms of **1**. Figure S3: Traces for the desorption kinetics of **2**. Table S7: Activation energies obtained for **1** and **2** at a different conversion levels. Detailed calculations for the network loading with various solvent molecules. Topos output files for **1** and **2**. CIF files for **1** and **2**. This material is available free of charge via the Internet at <http://pubs.acs.org>.

■ AUTHOR INFORMATION

Corresponding Author

*E-mail: gaelle.ramon@uct.ac.za. Fax: +27 21 650 5768. Tel: +27 21 650 5184.

Author Contributions

The manuscript was written through contributions of all authors. All authors have given approval to the final version of the manuscript. G.M. carried out the experimental work while S.A.B., G.R., and L.O. advised and guided on aspects of the project. G.R. wrote the first draft of manuscript which was then reviewed and refined with the support of S.A.B., L.O., and G.M.

Notes

The authors declare no competing financial interest.

■ ACKNOWLEDGMENTS

The authors thank the South African National Research Foundation (NRF) and the Swedish International Development Agency (SIDA) for financial support. G.M. is grateful for the financial support he received from the University of Cape Town Chemistry Equity Development Programme and the International Centre for Diffraction Data (ICDD): 2012 Ludo Frevel Crystallography Scholarship Award.

■ ABBREVIATIONS

34pba: 3-(4-pyridyl)benzoate; DMF: dimethylformamide; DSC: differential scanning calorimetry; TGA: thermogravimetric analyses; HSM: hot stage microscopy; E_a : activation energy; PXRD: powder X-ray diffraction; MOFs: metal organic frameworks; RT: room temperature; 44pba: 4-(4-pyridyl)benzoate; IR: infrared

■ REFERENCES

- (1) Jiang, H.-L.; Tatsu, Y.; Lu, Z.-H.; Xu, Q. *J. Am. Chem. Soc.* **2010**, *132*, 5586.
- (2) Wang, X.-S.; Ma, S.; Forster, P. M.; Yuan, D.; Eckert, J.; Lopez, J. J.; Murphy, B. J.; Parise, J. B.; Zhou, H.-C. *Angew. Chem., Int. Ed.* **2008**, *47*, 7263.
- (3) Galli, S.; Masciocchi, N.; Tagliabue, G.; Sironi, A.; Navarro, J. A. R.; Salas, J. M.; Mendez-Liñan, L.; Domingo, M.; Perez-Mendoza, M.; Barea, E. *Chem.—Eur. J.* **2008**, *14*, 9890.
- (4) Lu, Z.-Z.; Zhang, R.; Li, Y.-Z.; Guo, Z.-J.; Zheng, H.-G. *J. Am. Chem. Soc.* **2011**, *133*, 4172.
- (5) Gong, Y.; Zhou, Y.; Li, J.; Cao, R.; Qin, J.; Li, J. *Dalton Trans.* **2010**, *39*, 9923.

- (6) Bourne, S. A.; Moitsheki, L. *CrystEngComm* **2005**, *7*, 674.
- (7) Almesaker, A.; Bourne, S. A.; Ramon, G.; Scott, J. L.; Strauss, C. R. *CrystEngComm* **2007**, *9*, 997.
- (8) Rowsell, J. L. C.; Yaghi, O. M. *Angew. Chem., Int. Ed.* **2005**, *44*, 4670.
- (9) Ma, S.; Sun, D.; Ambrogio, M. W.; Fillinger, J. A.; Parkin, S.; Zhou, H. C. *J. Am. Chem. Soc.* **2007**, *129*, 1858.
- (10) Forster, P. M.; Burbank, A. R.; O'Sullivan, M. C.; Guillou, N.; Livage, C.; Férey, G.; Stock, N.; Cheetham, A. K. *Solid State Sci.* **2005**, *7*, 1549.
- (11) Stock, N.; Bein, T. *J. Mater. Chem.* **2005**, *15*, 1384.
- (12) Li, S.-L.; Tan, K.; Lan, Y.-Q.; Qin, J.-S.; Li, M.-N.; Du, D.-Y.; Zang, H. Y.; Su, Z.-M. *Cryst. Growth Des.* **2010**, *10* (4), 1699.
- (13) Forster, P. M.; Burbank, A. R.; Livage, C.; Férey, G.; Cheetham, A. K. *Chem. Commun.* **2004**, 368.
- (14) Cheetham, A. K.; Rao, C. N. R.; Feller, R. K. *Chem. Commun.* **2006**, 4780.
- (15) Davies, K.; Bourne, S. A.; Oliver, C. L. *Cryst. Growth Des.* **2012**, *12*, 1999.
- (16) Davies, K.; Bourne, S. A.; Öhrström, L.; Oliver, C. L. *Acta Crystallogr. Sect. B: Struct. Sci.* **2012**, *68*, 528.
- (17) Tian, Y.-Q.; Chen, Z.-X.; Weng, L.-H.; Guo, H.-B.; Gao, S.; Zhao, D. Y. *Inorg. Chem.* **2004**, *43*, 4631.
- (18) Dai, F.; He, H.; Sun, D. *Inorg. Chem.* **2009**, *48*, 4613.
- (19) Katz, M. J.; Ramnial, T.; Yu, H.-Z.; Leznoff, D. B. *J. Am. Chem. Soc.* **2008**, *130*, 10662.
- (20) Kanoo, P.; Gurunatha, K. L.; Maji, T. K. *Cryst. Growth Des.* **2009**, *9*, 4147.
- (21) Moulton, B.; Zaworotko, M. J. *Chem. Rev.* **2001**, *101*, 1629.
- (22) Zhang, J.-P.; Huang, X.-C.; Chen, X.-M. *Chem. Soc. Rev.* **2009**, *38*, 2385.
- (23) Makal, T. A.; Yakovenko, A. A.; Zhou, H.-C. *J. Phys. Chem. Lett.* **2011**, *2*, 1682.
- (24) Bourne, S. A. In *Supramolecular Chemistry: From Molecules to Nanomaterials*; Gale, P. A., Steed, J. W., Eds.; John Wiley & Sons, Ltd, U.K, 2012; Vol. 6, pp 3121–3132.
- (25) Batten, S. R.; Champness, N. R.; Chen, X. M.; Garcia-Martinez, J.; Kitagawa, S.; Öhrström, L.; O'Keeffe, M.; Suh, M. P.; Reedijk, J. *CrystEngComm* **2012**, *14*, 3001.
- (26) *SAINT*, Version 7.60a; Bruker AXS Inc: Madison, WI, USA, 2006.
- (27) Sheldrick, G. M. *SADABS*, Version 2.05; 2007
- (28) Sheldrick, G. M. *Acta Crystallogr. Sect. A: Found. Crystallogr.* **2008**, *64*, 112.
- (29) Sheldrick, G. M. *SHELXL-97, Program for Crystal Structure Solution*, 1997.
- (30) Barbour, L. J. *J. Supramol. Chem.* **2001**, *1*, 189.
- (31) Macrae, C. F.; Bruno, I. J.; Chisholm, J. A.; Edgington, P. R.; McCabe, P.; Pidcock, E.; Rodriguez-Monge, L.; Taylor, R.; van de Streek, J.; Wood, P. A. *J. Appl. Crystallogr.* **2008**, *41*, 466–470 Mercury 3.0 version.
- (32) Friedrichs, O. D. *SYSTRE 1.1.4beta*, <http://gavrog.sourceforge.net/>, 2007.
- (33) Blatov, V. A.; Peaskov, V. *Acta Crystallogr. Sect. B Struct. Sci.* **2006**, *62*, 457. Blatov, V. A. Ac. Pavlov St. 1, 443001, Samara, Russia, TOPOS 4.0, <http://www.topos.ssu.samara.ru/>, accessed May 2012.
- (34) O'Keeffe, M.; Peskov, M. A.; Ramsden, S.; Yaghi, O. M. *Acc. Chem. Res.* **2008**, *41*, 1782. O'Keeffe, M.; Yaghi, O. M.; Ramsden, S. Australian National University Supercomputer Facility, Reticular Chemistry Structure Resource, <http://rcsr.anu.edu.au/>, 2009.
- (35) Soft Imaging System GmbH: Digital solutions for Imaging and Microscopy, Version 3.1 for Windows, 1987–2000.
- (36) Borchardt, H. J.; Daniels, F. *J. Am. Chem. Soc.* **1957**, *79*, 41.
- (37) Lee, C.; Mellot-Draznieks, C.; Slater, B.; Wu, G.; Harrison, W. T. A.; Rao, C. N. R.; Cheetham, A. K. *Chem. Commun.* **2006**, 2687.
- (38) Bernstein, J.; Davey, R. J.; Henck, J.-O. *Angew. Chem., Int. Ed.* **1999**, *38* (23), 3440.
- (39) Beauvais, L. G.; Shores, M. P.; Long, J. R. *J. Am. Chem. Soc.* **2000**, *122*, 2763.

- (40) Martini, D.; Pellei, M.; Pettinari, C.; Skelton, B. W.; White, A. H. *Inorg. Chim. Acta* **2002**, 333 (1), 72.
- (41) Nakamoto, K. In *Infrared and Raman Spectra of Inorganic and Coordination Compounds, Applications in Coordination, Organometallic, and Bioinorganic Chemistry*; Hoboken, NJ, USA: Wiley, 2009; pp 64–66.
- (42) Ozawa, T. *Bull. Chem. Soc. Jpn.* **1965**, 38, 1881.
- (43) Flynn, J. H.; Wall, L. A. *J. Polym. Sci. Part B: Polym. Lett.* **1966**, 4, 323.
- (44) Bourne, S. A.; Gifford-Nash, K. L.; Toda, F. *J. Mol. Struct.* **1999**, 474, 223.
- (45) Jacobs, A.; Masuku, N. L. Z.; Nassimbeni, L. R.; Taljaard, J. H. *CrystEngComm* **2008**, 10, 322.
- (46) Jacobs, A.; Nassimbeni, L. R.; Nohako, K. L.; Su, H.; Taljaard, J. H. *Cryst. Growth Des.* **2008**, 8, 1301.
- (47) Mehlana, G.; Bourne, S. A.; Ramon, G. *Dalton Trans.* **2012**, 41, 4224.

■ NOTE ADDED AFTER ASAP PUBLICATION

This paper was published to the Web on January 8, 2013, with an error to Table 2. The corrected version was reposted on January 11, 2012.